

URTeC: 2652022

Simultaneous inversion for microseismic event location and velocity model in Vaca Muerta Formation

Zhishuai Zhang*, University of California, Berkeley; Jing Du, and Fuchun Gao, Total E&P R&T, Houston

Copyright 2017, Unconventional Resources Technology Conference (URTeC) DOI 10.15530/urtec-2017-2652022

This paper was prepared for presentation at the Unconventional Resources Technology Conference held in Austin, Texas, USA, 24-26 July 2017.

The URTeC Technical Program Committee accepted this presentation on the basis of information contained in an abstract submitted by the author(s). The contents of this paper have not been reviewed by URTeC and URTeC does not warrant the accuracy, reliability, or timeliness of any information herein. All information is the responsibility of, and, is subject to corrections by the author(s). Any person or entity that relies on any information obtained from this paper does so at their own risk. The information herein does not necessarily reflect any position of URTeC. Any reproduction, distribution, or storage of any part of this paper without the written consent of URTeC is prohibited.

Summary

Microseismic monitoring of hydraulic fractures is an important technology for far-field fracture diagnostics. It provides us hydraulic fracture geometry and its growth behavior vs. time. Getting accurate microseismic event location is important to interpretation, and velocity model plays a key role in obtaining event location. However, due to the limited number of perforation shots, limited ray coverage, and identifying / classifying different phase arrivals in the perforation data, building a reasonable velocity model is very challenging. In this paper, we present a field case study, in which we apply the Bayesian inference algorithm to simultaneously invert for microseismic event locations, origin times, and velocities. The stability of the simultaneous inversion is tested with a cross-validation and the accuracy of the locations is cross-verified with P-wave polarization for looking at the event incidence angle at each receiver. The inversion results were compared with a traditional location result located using a velocity model, which is built from perforation shot data only. It shows that the simultaneous inversion has improved microseismic event location.

With the algorithm demonstrated in this paper, we can not only perform microseismic monitoring to fracturing treatments where no perforation data is available; but also improve the microseismic event location when we do have perforation data. In addition, this algorithm could be applied to long term reservoir monitoring with microseismic array where we do need to retrieve velocity information from the microseismic events themselves.

Introduction

Multistage fracturing technique, together with horizontal drilling, make production from organic-rich shale possible. Microseismic monitoring of hydraulic fractures has been an important technology for far-field fracture diagnostics (Eisner and Le Calvez, 2007; Maxwell, 2014). It can provide us hydraulic fracture geometry and its growth behavior vs. time. Getting accurate microseismic event location is important to interpretation. Various methods originally developed for earthquake location have been used for microseismic event location, such as travel-time inversion (Aki and Richards, 1980; Rutledge and Phillips, 2003), double-difference method (Waldhauser and Ellsworth, 2000), coherence scanning (Drew et al., 2005; Duncan and Eisner, 2010), time-reverse imaging (Artman et al., 2010; Artman and Witten, 2011), and waveform inversion (Song and Toksöz, 2011). In almost all of these methods, the velocity model plays a key role in event location (Eisner et al., 2009; Maxwell, 2009; Warpinski, 2009; Gesret et al., 2015). However, due to the limited number of perforation shots, limited ray coverage, and difficulty of picking S-wave arrivals reliably in the perforation data, building a reasonable velocity model is usually very challenging (Maxwell, 2014).

Simultaneous inversion of earth model and earthquake locations has been successfully used in earthquake seismology (Douglas, 1967). The limitation of acquisition geometry and low S/N make it challenging to apply this idea to microseismic data. There are only a few studies about simultaneous inversion for microseismic event locations. Jansky et al. (2010) used the neighborhood algorithm to simultaneously invert for microseismic event

locations and a velocity model in downhole survey. Zhang et al. (2009) have used double-difference tomography method to study the induced seismicity monitored with geophones deployed in five monitoring wells. Li et al. (2013) and Li et al. (2014) have inverted for Thomsen parameters using P- and S-wave arrival time information. Grechka et al. (2011) estimated key stiffness coefficients that can be well constrained by assuming a homogeneous earth model. However, the study of simultaneous inversion in the microseismic industry is still very limited, especially for the cases where acquisition geophones are constrained within one single well.

Bayesian inference has been widely used in subsurface inverse problems (Tarantola and Valette, 1982; Tarantola, 2005; Myers et al., 2007; Myers et al., 2009; Poliannikov et al., 2013; Poliannikov et al., 2014; Zhang et al., 2014). We have developed a Bayesian inference framework to simultaneously invert for microseismic event location and velocity model, and successfully applied it to a microseismic data set obtained from shallow borehole stations (Zhang et al., 2017). Studies show that a velocity model can be constructed with relatively high confidence using microseismic data only. The Bayesian inference provides an efficient way to quantify the uncertainty of the microseismic event location estimation. It is also able to capture the correlation between various model parameters, such as velocity model parameters and microseismic event locations.

In this paper, we applied the simultaneous inversion algorithm to a microseismic data set obtained by an array of geophones in a single vertical well within Vaca Muerta Formation at Neuquén, Argentina. Bayesian inference is successful in integrating various information in the simultaneous inversion process for this data set. The uncertainty of the inversion is obtained and compared with an arrival time misfit map. Analyses with various data subsets, perforation shots, and P-wave angle of incidence show the effectiveness and stableness of the method. A comparison with a traditional location result located using a velocity model built from perforation shot data shows the superiority of simultaneous inversion. The simultaneous inversion minimizes the requirement of a predetermined velocity model and also provides the possibility to study the time lapse change of the earth model due to hydraulic fracturing.

The structure of the remainder of this paper is as follows: we first give an overview of the simultaneous inversion algorithm we developed. Then we present the microseismic survey and the initial model we used for the simultaneous inversion. We applied the simultaneous inversion to a data set from Vaca Muerta formation in Neuquén, Argentina and verify the results with various analyses. Finally, we conclude with the discussion of the limitation and next step of this work.

Method

We have developed a Bayesian inference framework to simultaneously invert for microseismic event locations and velocity model for a shallow borehole survey (Zhang, Rector and Nava, 2017). In this section, we present the application of this method to a typical microseismic acquisition geometry, that is, the microseismic monitoring with a geophone array deployed within a single vertical well.

As with the common practice in microseismic industry, we assume a 1D layered isotropic velocity model for the microseismic event location in this study. Under this assumption, along with the fact that the geophones are in a strict vertical monitoring well, the 3D microseismic location problem using arrival times can be decoupled into a 2D problem and an azimuth estimation problem. In the 2D problem, the parameters to characterize a microseismic event location are the horizontal distance between the event and the geophone array, and the elevation of the event. These two parameters, along with the origin time of the event, are to be estimated during the simultaneous inversion. The other set of parameters to be simultaneously estimated are the parameters to characterize the velocity model. The parameterization of the earth model is a challenging problem. More parameters will decrease the parameterization error, however, may lead to an ill-posed problem. The velocity model parameter set we use in this study is comprised of P- and S-wave velocities at all layers. However, depending on the data quality, ray path coverage of the events, and availability of the prior information, additional parameters, including layer boundaries, anisotropic parameters, may be used. In this paper, given the availability and quality of microseismic data, for a system with N microseismic events and M layers, we use a model parameter set \mathbf{m} , which is a vector of length $3N + 2M$:

$$\mathbf{m} = [\mathbf{x}_1, \mathbf{x}_2, \dots, \mathbf{x}_i, \dots, \mathbf{x}_N; V_{P1}, V_{S1}, V_{P2}, V_{S2}, \dots, V_{Pj}, V_{Sj}, \dots, V_{PM}, V_{SM}]^T, \quad (1)$$

where $\mathbf{x}_i = [H_i, D_i, t_i]$ are the horizontal distance (H_i), vertical coordinate (D_i), and origin time (t_i) of the i th microseismic event. V_{Pj} and V_{Sj} are the P- and S-wave velocities of the j th layer.

The measurement \mathbf{d}_{obs} includes any available P- and/or S-wave arrival times for each event at each station. The forward operator $\mathbf{g}(\cdot)$ is to predict the observable parameters using model parameters \mathbf{m} . Specifically, it calculates the travel times from microseismic event locations to geophone locations using a ray tracing method.

According to the inverse problem theory (Tarantola, 2005) under a Gaussian probability density assumption, the posterior probability density of the model parameters is given by

$$\sigma_M(\mathbf{m}) = c \exp \left\{ -\frac{1}{2} [\mathbf{g}(\mathbf{m}) - \mathbf{d}_{\text{obs}}]^T \mathbf{C}_D^{-1} [\mathbf{g}(\mathbf{m}) - \mathbf{d}_{\text{obs}}] - \frac{1}{2} (\mathbf{m} - \mathbf{m}_{\text{prior}})^T \mathbf{C}_M^{-1} (\mathbf{m} - \mathbf{m}_{\text{prior}}) \right\}, \quad (2)$$

where $\mathbf{m}_{\text{prior}}$ is the prior mean value of the model parameters. The covariance matrix \mathbf{C}_D is the addition of observation and parameterization uncertainty covariance matrices \mathbf{C}_d and \mathbf{C}_T . \mathbf{C}_M is the covariance matrix of the prior information. c is a normalization constant. A detailed discussion of equation (2) is presented by Tarantola (2005) and Zhang, Rector and Nava (2017).

Following the discussion of Zhang, Rector and Nava (2017), we use the Maximum A Posterior (MAP) estimation \mathbf{m}_{MAP} , along with its covariance matrix $\mathbf{C}_{\text{m,MAP}}$ under a Gaussian assumption to characterize the posterior probability density of the model parameters:

$$\mathbf{m}_{\text{MAP}} = \underset{\mathbf{m}}{\text{argmax}} \sigma_M(\mathbf{m}), \quad (3)$$

and

$$\mathbf{C}_{\text{m,MAP}} = \mathbf{C}_M - \mathbf{C}_M \mathbf{G}_{\text{MAP}}^T (\mathbf{G}_{\text{MAP}} \mathbf{C}_M \mathbf{G}_{\text{MAP}}^T + \mathbf{C}_D)^{-1} \mathbf{G}_{\text{MAP}} \mathbf{C}_M, \quad (4)$$

where \mathbf{G}_{MAP} is the sensitivity matrix with elements $G_{ij} = \frac{\partial g_i}{\partial m_j}$ at the MAP point.

Even though MAP point and the covariance matrix approximation are exact only when all the information are of Gaussian type and the operator $\mathbf{g}(\cdot)$ is linear, which is usually not the case, this approximation is efficient in terms of calculation and is normally a reasonable representation of the posterior probability density function. The \mathbf{m}_{MAP} can be achieved with a Gauss-Newton method.

Microseismic survey project overview

The hydraulic fracturing was performed in the Vaca Muerta Formation at Neuquén, Argentina and the acquisition geometry is shown in Figure 1. The Vaca Muerta Formation consists of an upper (elevation of -1985 m to -2135 m) and a lower (elevation of -2135 m to -2305 m) member. It is overlain by the Quintuco Formation (elevation of -1221 m to -1985 m) and is above the Tordillo Formation (below the elevation of -2305 m). The horizontal stimulation well was drilled perpendicular to the expected fracture azimuth in the lower Vaca Muerta and completed as a cemented lateral using a plug-and-perf. A total of five hydraulic fracturing treatment stages were performed. Due to an operational issue in the field, the Stage 1 was pumped twice, which we called them two sub-stages (Stage 1A and Stage 1B).

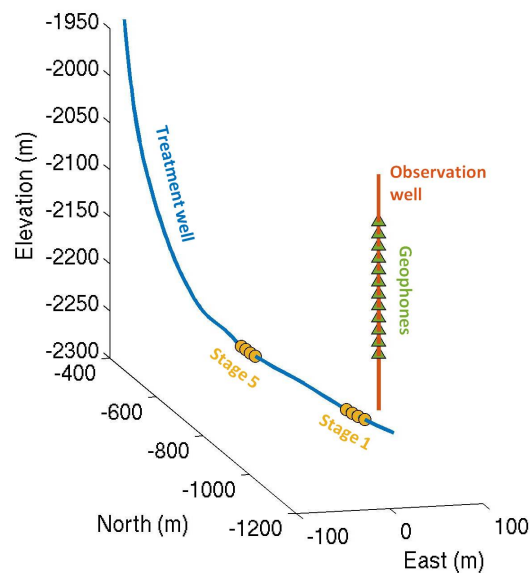


Figure 1: Stimulation project and microseismic survey setup. A total of five hydraulic fracturing treatment stages were performed in the horizontal stimulation well. Microseismic data from Stage 1 and Stage 5 are acquired and studied. The microseismic monitoring was carried out by a 24-tool, 12-level double stacked receiver array positioned in an adjacent vertical observation well.

The microseismic data was acquired by a 24-tool, 12-level double stacked receiver array positioned in the adjacent vertical observation well. The sampling rate of the recorded data is 0.25 ms. Among the five stimulation stages, microseismic data from only two stages, that is, Stage 1 and Stage 5, were monitored and processed by a contractor. The geophone array monitoring Stage 5 is approximately 100 m shallower than that for Stage 1. The numbers of microseismic events reported by the contractor in Stage 1A, 1B, and 5 are respectively 404, 884, and 377. For all the perforation shots in the five fracturing stages, only three shots for Stage 1 were recorded by the borehole microseismic array due to various reasons.

The microseismic data has been processed by a contractor using standard industrial practice. To locate these microseismic events, first a 1D layered isotropic velocity model was built basing on a sonic log, then was calibrated with perforation shots. The microseismic events were located by minimizing the misfit between the picked arrival times and the arrival times predicted using these predetermined velocity models. The forward modeling was conducted by solving the Eikonal equation for the first arrivals, which might be direct or refracted waves.

Preprocessing and initial model

As a preparation for the simultaneous inversion, we selected 76 events from Stage 1 and 55 events from Stage 5 with relatively high data quality and good ray path coverage for us to re-pick the arrival times of P- and S-waves reasonably well. To ensure the quality of the pickings, we calculate the angle of incidence of each event-geophone pair with ray tracing. Then, using this angle of incidence, along with the azimuth obtained by the contractor with P-wave polarization on the horizontal plane, we rotated the waveforms to separate P-, SH-, and SV-wave components. We picked P-wave arrival times from the P-wave component and S-wave arrival times from the SH-wave component whenever we were able to do so. We used our own pickings for the following processing unless stated otherwise.

To reduce the number of velocity model parameters in the simultaneous inversion while keep the theoretical errors introduced by parameterization reasonably small, we built a 9 layers homogeneous prior/initial model for Stage 1 (Figure 2) and an 11 layers model for Stage 5 (not shown here for simplicity). The layer interfaces are positioned based on the sonic logs, geological information, and the contractor's velocity model. The prior velocities of all the layers are 3500 m/s for P-wave and 2100 m/s for S-wave. Since we assume we don't have much prior information of the velocity model in this case, we can use relatively large uncertainties to make sure the velocity model is estimated mainly based on microseismic data and not biased by the prior information. Thus, we use 2000 m/s, which is a

relatively large value, as the standard deviations of these velocities. The same philosophy applied for the uncertainties of other prior information such as prior event locations and origin times.

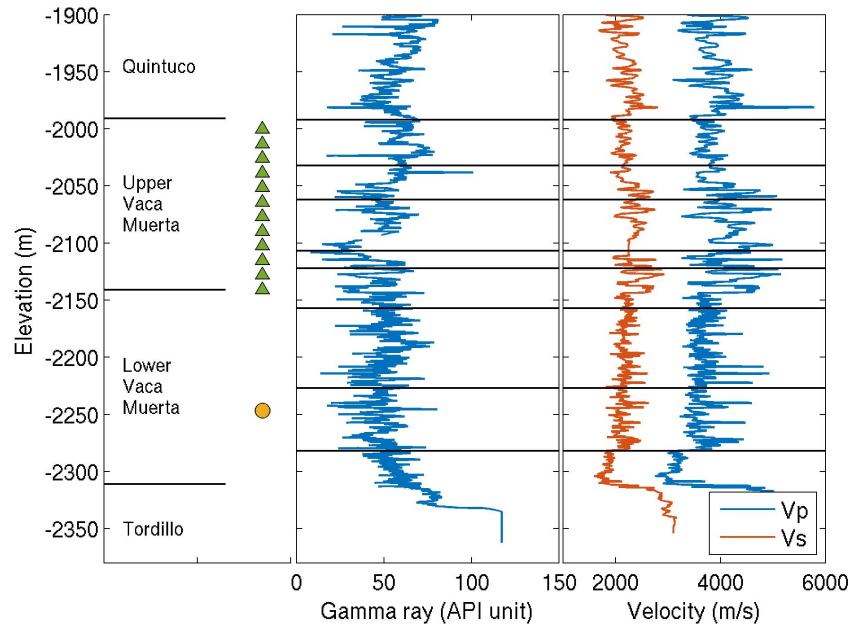


Figure 2: The prior/initial velocity model we used for simultaneous inversion in Stage 1 is a homogeneous multilayer model. The layer interfaces are positioned based on the sonic logs, geological information, and the contractor's velocity model. The green triangles and yellow circle on the left indicate the elevations of geophones and perforation shots respectively. The black lines on the logs indicate the velocity model layer interfaces.

The prior horizontal distances between geophone array and microseismic events are all 200 m for Stage 1 events and 400 m for Stage 5 events. We assigned its standard deviation to be 1000 m, which means we barely have any information about the event locations before the inversion. This choice of parameters will ensure the inversion result is insensitive to the prior information and the initial model. For the same reason, we used a prior elevation of -2250 m and standard deviation of 1000 m for the microseismic events in both stages. In the experiments using the locations of perforation shots as constraints, we used a standard deviation of 0.5 m for both horizontal distance and elevation of these perforation shots. Figure 3 shows the prior microseismic event location and the prior velocity model for Stage 1. The plot of prior information for Stage 5 is not shown here for simplicity. The minimization of the objective function started with the prior model as the initial model in all of the experiments. The prior origin times are 0.2 s before the first P-wave arrival time with a standard deviation of 8.0 s. We use a standard deviation of 1.5 ms to represent the observation and parameterization errors used to calculate C_D in equation (2).

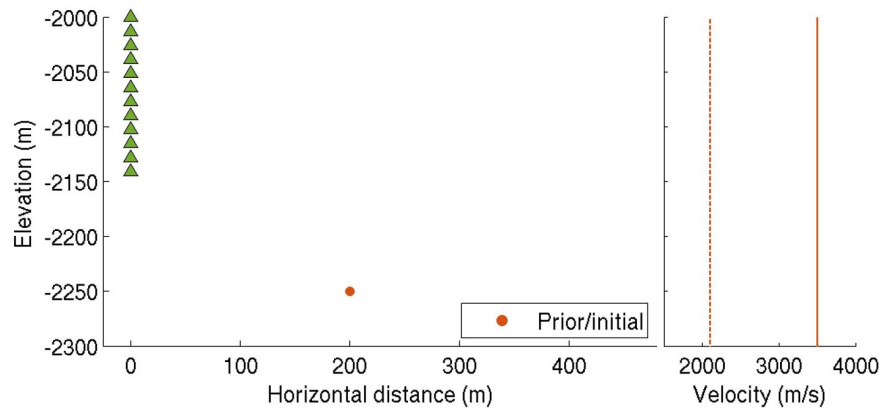


Figure 3: Prior/initial microseismic event locations and velocity model. The standard deviation of the prior event location is 1000 m in both horizontal and vertical directions. The standard deviation of the prior velocity model is 2000 m/s for both P- and S-waves.

Inversion result

Relocation with the contractor provided velocity model

For the purpose of comparison, we first locate the 76 microseismic events in Stage 1 with the velocity model provided by the contractor using traditional location method. Specifically, we used the same program as the simultaneous inversion but didn't include the velocity model in the model parameters to be updated. The location result is shown in Figure 4 together with the reference location catalog provided by the contractor. While there are indeed some differences between these two results, they show similar trend. The differences are mainly due to the differences in arrival time pickings, forward modeling algorithms, and inversion criteria. They are much smaller than the differences introduced by the forthcoming simultaneous inversion in Figure 5. Thus, we use this relocation result with the provided velocity model as a representation of the result of traditional location method.

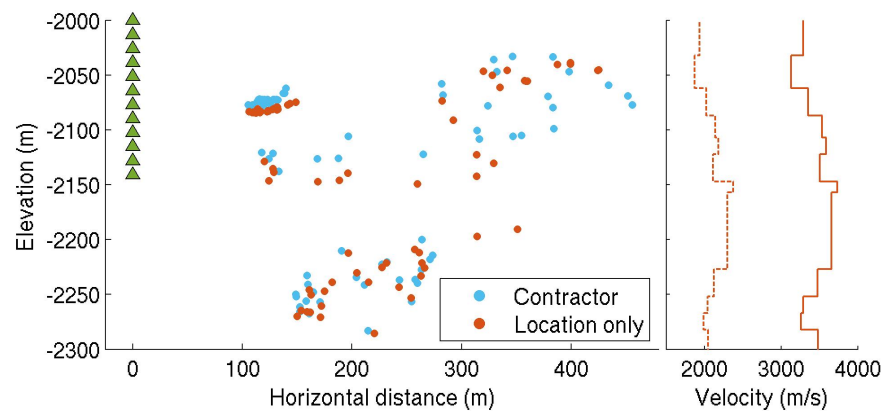


Figure 4: Event locations (orange dots) estimated with the velocity model provided by the contractor using traditional method and the location catalog provided by the contractor (light blue dots). These two location results show similar trend. The right figure is the velocity model (solid line for Vp and dashed line for Vs) provided by the contractor.

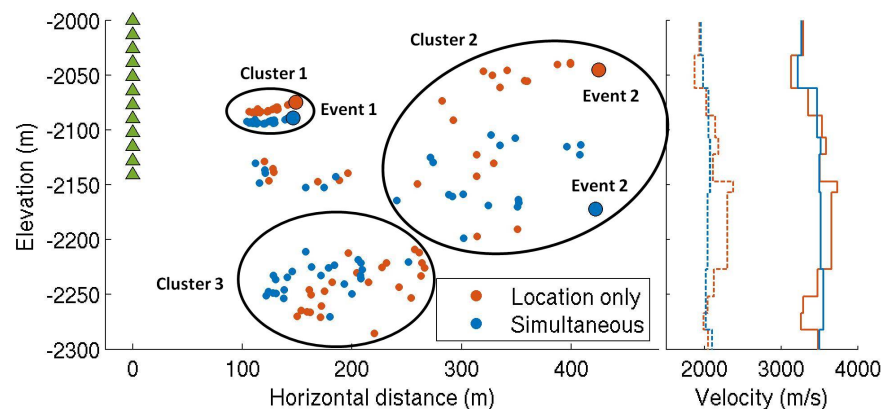


Figure 5: Events locations with our simultaneous inversion algorithm (blue dots) and those estimated with the velocity model provided by the contractor using traditional method (orange dots). The difference between these two results is relatively large. The right figure is the velocity model estimated with our simultaneous inversion (blue) and the one provided by the contractor (orange). The solid line is for Vp and the dashed line is for Vs.

Simultaneous inversion result

We inverted these 76 event locations, origin times, and the velocity model with the simultaneous inversion algorithm. The result is shown in Figure 5 along with the traditional location result using the provided velocity model. There are relatively large differences between these two results. Firstly, the small dense event cluster, that is cluster 1, was shifted to a lower position and is flatter than the original cluster. Secondly, the large event cluster 2 was shifted from the elevation of -2060 m to about -2150 m. In addition, the event cluster 3 was shifted towards the left.

To understand the differences between these two results, we plotted the picks and predicted arrival times of two events with relatively large difference (event 1 and event 2 in Figure 5) as shown in Figure 6 and Figure 7. The waveforms have been rotated to show only the P- and SH-wave component. The amplitude scales of P- and SH-wave components are different due to the relatively large amplitude ratio between S-wave and P-wave, thus, even though the S-wave residuals in the P-component are comparable to the P-wave amplitude, they are significantly smaller than the SH-wave. From Figure 6, we can see the predicted arrival times of the traditional location-only method have relatively large differences from the true P-wave arrival pickings. The same problem is more significant for event 2 as shown in Figure 7. The predicted arrival times of the traditional location-only method is unable to capture the moveouts of the real arrival times. However, the simultaneous inversion algorithm was able to implicitly detect and correct these misfits by updating the velocity model using microseismic arrival time information as shown by the improved match between the predicted arrival times of the simultaneous inversion and the arrival time pickings.

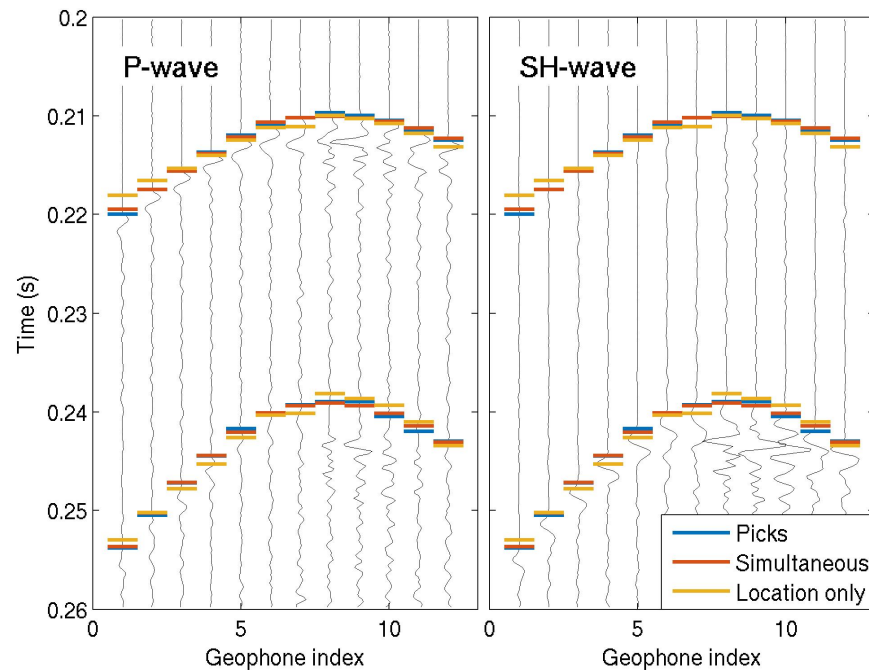


Figure 6: The P- and SH-component waveform of event 1 in Figure 5. Blue lines stand for manually picked arrival time. Orange lines are arrival time predictions of the simultaneous inversion method. Yellow lines are arrival time predictions of the traditional location method using the contractor's velocity model. The P- and S-wave arrival times predicted by the traditional method are unable to match the picks with the provided velocity model. Our simultaneous inversion was able to construct a velocity model whose arrival time predictions match the picks relatively well.

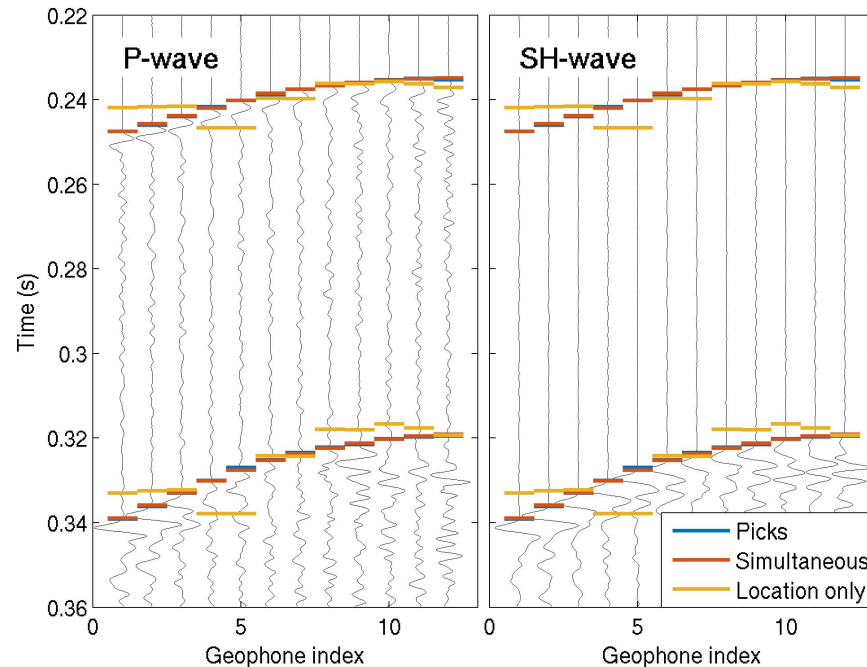


Figure 7: The same as Figure 6 but for event 2. The misfit between the predicted arrival times of the traditional location method and the real pickings is more significantly for event 2.

We also compared the root-mean-square (RMS) misfit of the arrival times of all these 78 events in Table 1. The RMS misfit using provided velocity model is 1.68 ms while that using our simultaneous inversion is only 0.47 ms. This large decrease in RMS misfit attributes to the improvement in arrival time match like Figure 6 and Figure 7. It shows the superiority of the simultaneous inversion over the traditional location-only method. We can draw similar conclusion from the histogram of the misfit between observation and prediction (Figure 8). The misfit histogram of the simultaneous inversion is much more concentrated around zero, which means the velocity model estimated with the simultaneous inversion is a better representation of the true model.

Table 1: RMS misfits of various experiments.

Events	Velocity model type	RMS misfit (ms)		
		P	S	P and S
76 events	Contractor	1.31	1.98	1.68
	76 events estimated	0.42	0.51	0.47
First 38 events	First 38 events estimated	0.38	0.48	0.44
	Second 38 events estimated	0.41	0.50	0.46
Second 38 events	Second 38 events estimated	0.44	0.52	0.48
3 perfs	Contractor	1.38	1.20	1.29
	76 events estimated	0.99	0.76	0.88
76 events and 3 perfs	76 events and 3 perfs estimated	0.43	0.53	0.49

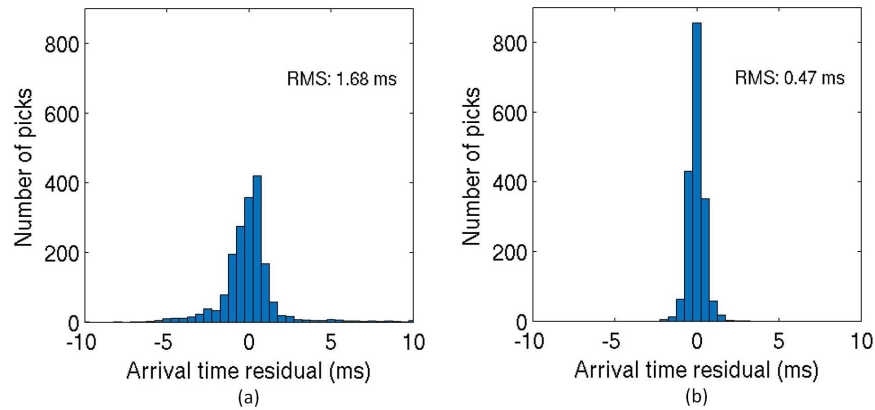


Figure 8: The histogram of the misfit between observed and predicted arrival times. The result using the simultaneous inverted velocity model (b) is more concentrated around zero compared with the one using the provided velocity model (a), which means the simultaneous inverted velocity model is better at predicting the arrival time observations.

One way to reduce the velocity estimation uncertainty is using the perforation shots information as a constraint. We carried out the simultaneous inversion with P- and S-wave arrival times of both perforation shots and microseismic events. The perforation shots locations were provided as prior information as discussed in the section of prior information and the initial model for estimation. The comparison between the locations with and without perforation shots as a constraint is shown in Figure 9. The perforation shots didn't significantly affect the event locations at higher elevation since the velocity model in this area has already been successfully estimated from the microseismic data. However, for those events near the perforation shots, the perforation shots improved their event location estimation. The effect of perforations shots can also be seen from the velocity model comparison on the right of Figure 9. The V_p values of the two layers below the geophone array have been significantly changed by the perforations shots while those of other layers remains similar with our previous estimation.

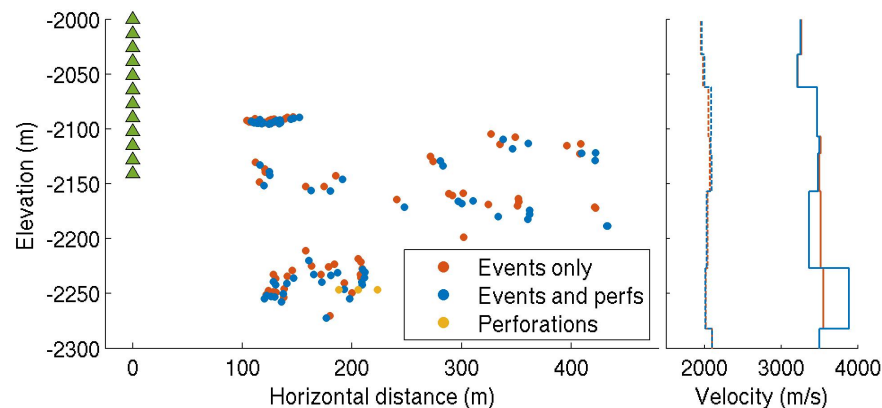


Figure 9: The comparison between simultaneous inversion result with (blue) and without (orange) perforation shots as a constraint. The perforation shots mainly affect the locations of events near the perforations. This is due to the improvement in velocity model below the geophone array brought by the perforations shot data. The right figure is the velocity model estimated with microseismic events only (orange) and the one estimated with both perforation shots and microseismic events (blue). The solid line is for V_p and the dashed line is for V_s .

Uncertainty analysis

One of the advantages of Bayesian inversion is that it can provide an estimation of posterior model parameter uncertainty as shown in Figure 10 and Figure 11. Figure 10 shows the 95 % confidence region predicted by the Bayesian inference. Figure 11 is the posterior velocity (P-wave only, the velocity model uncertainty for S-wave shares similar trend with that of P-wave, thus, not shown here for simplicity) model uncertainty of our estimation along with the ray paths of several representative events. The velocity model uncertainty around the geophone is relatively small, which means we have high confidence on the velocity model estimated for this region. The velocity uncertainty of the area below the geophone array is relatively large due to poor ray path coverage of this area. We also compared the uncertainty estimation of a representative microseismic event with the arrival time misfit map,

which is commonly used to quantify location uncertainty, in Figure 12. This uncertainty estimation matches the prediction of the Bayesian inference relatively well, and it verified the effectiveness of Bayesian inference in terms of uncertainty analysis.

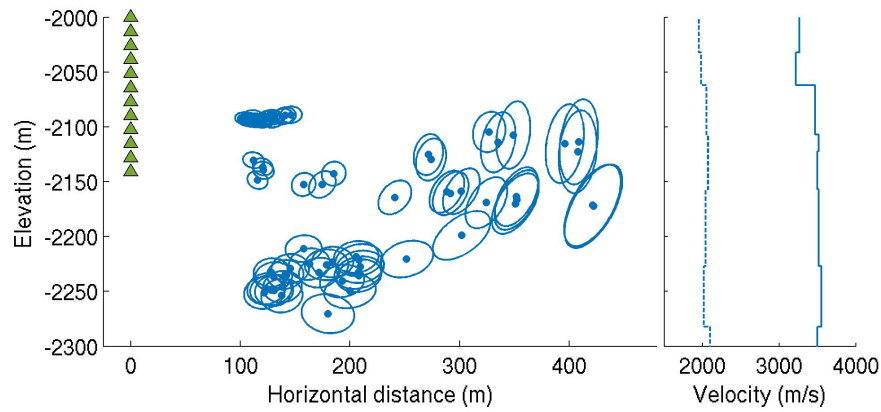


Figure 10: The MAP estimated locations of simultaneous inversion and the 95 % confidence regions (ellipses) predicted by the Bayesian inference. The accuracy of estimation is mainly dependent on the relative location of the event with respect to the geophone array.

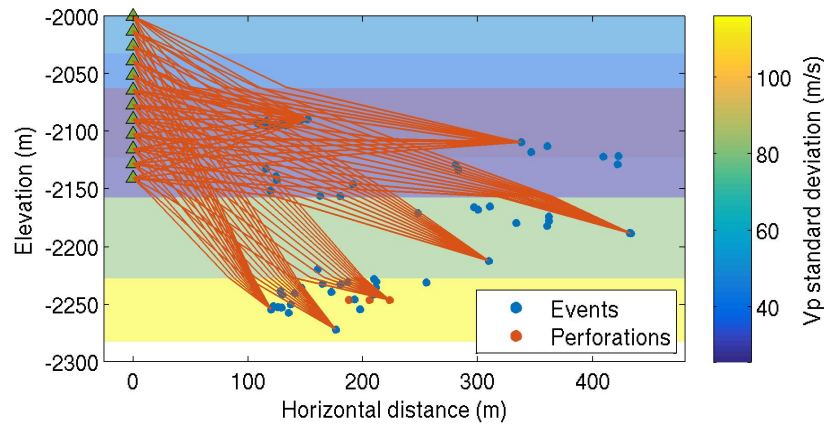


Figure 11: The ray paths of several representative events. The background is standard deviation of the velocity model estimation uncertainty. The uncertainty of the velocity model tends to be larger as the model goes deeper.

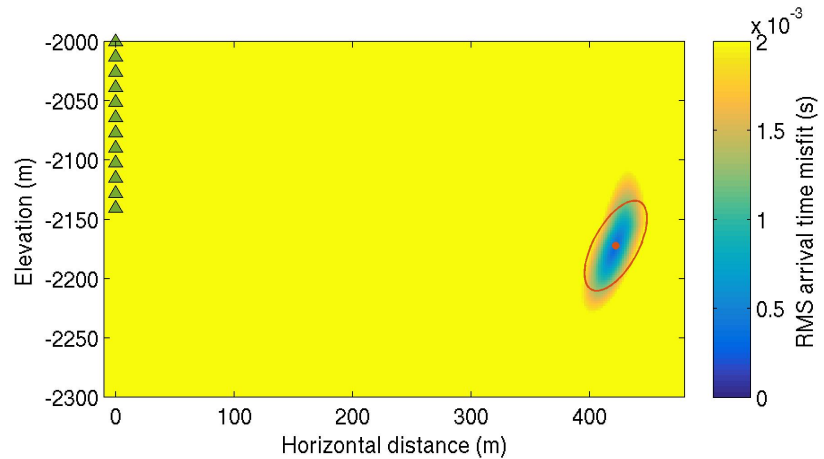


Figure 12: Comparison between the arrival time misfit, which is a traditional way to quantify location uncertainty, and the uncertainty prediction of the Bayesian inference. The relatively good match between these two results verified the effectiveness of Bayesian inference in terms of estimation uncertainty analysis.

Downloaded 05/06/18 to 171.66.208.145. Redistribution subject to SEG license or copyright; see Terms of Use at http://library.seg.org/

Location result verification

To prove the estimation is stable and our reduction in RMS misfit is not a result of over-fitting, we randomly subdivide our data into two subsets with 38 events each. The event locations and velocity models estimated with these two subsets are shown in Figure 13. The patterns of these two event subsets compare well with each other. The two velocity models match well, especially at the elevation of the geophone array. In addition, as shown by Table 1, the RMS misfits of arrival times for these two events subsets are respectively 0.44 ms and 0.48 ms. This is comparable to the RMS misfit of 0.47 ms using the whole 76 events set. Then, using the velocity model estimated from subset two, we located the events from subset one with the traditional location method. The location result is compared with that of the simultaneous inversion of subset one in Figure 14. We can see these two results compare relatively well to each other. These tests and observations confirm the reduction in arrival time residual is not a result of over-fitting and the simultaneous inversion algorithm is stable for this data set.

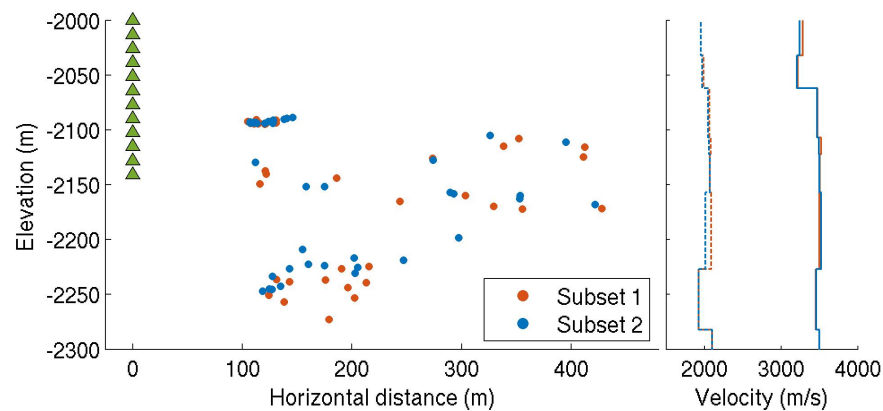


Figure 13: Microseismic event locations of two independent subsets of data. They share similar locations patterns and the velocity models estimated by these two subsets of data are similar, especially at the elevation of the geophone array. The right figure is the velocity model estimated with event subset 1 (orange) and the one estimated with event subset 2 (blue). The solid line is for V_p and the dashed line is for V_s .

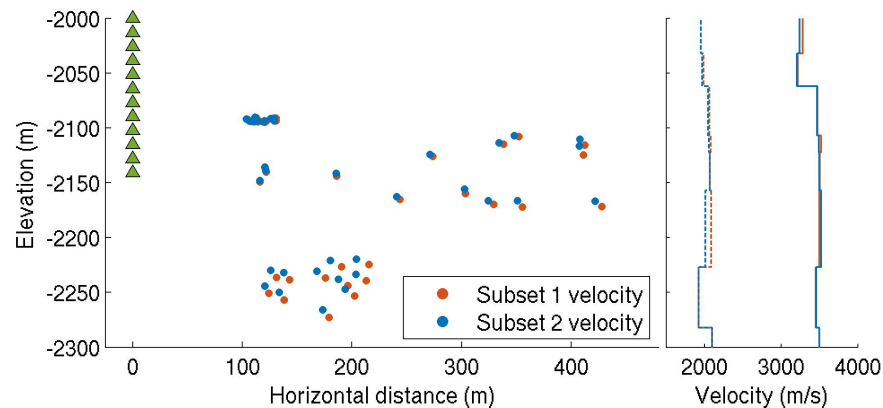


Figure 14: Subset one events locations estimated using the velocity models from subset one data (orange) and subset two data (blue). These two results match relatively well. The right figure is the velocity model estimated with event subset 1 (orange) and the one estimated with event subset 1 (blue). The solid line is for V_p and the dashed line is for V_s .

Another way to quantify the location uncertainty is locating the perforation shots to compare with their true locations. We estimated the perforation shot locations with both the provided velocity model and our simultaneous inverted velocity model using the 76 microseismic events (Figure 15). Those estimated with our model is nearer to the true perforation shot locations comparing with those using the provided model. The mismatch between the result using the contractor's velocity model and the true locations is due to the difference between our pickings and the contractor's. The RMS misfit of the result using our model is also smaller as shown by Table 1. Comparing these two results, we find that the perforation shot locations are significantly shifted away from the geophone array horizontally by using the velocity model provided. This is the same phenomena for the event cluster 3 in Figure 5. The perforation shots are at the same area with the event cluster 3, and this shows that the events tend to be

estimated further from their true locations with the provided velocity model. And the simultaneous inversion is capable to construct a relatively accurate velocity model, thus, improve the microseismic event location accuracy.

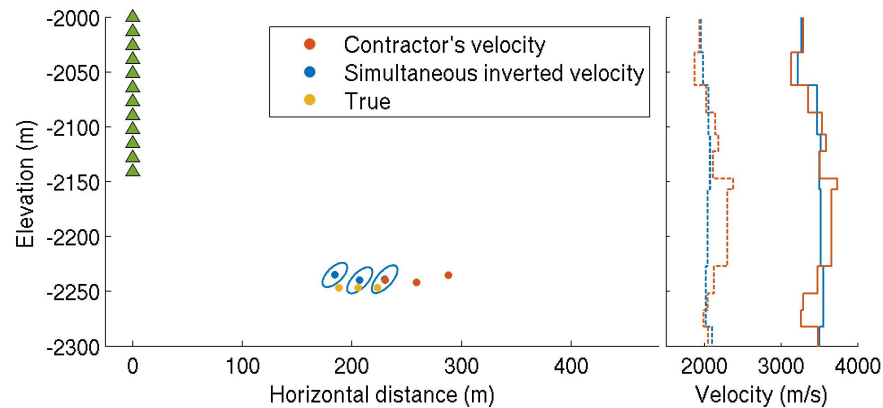


Figure 15: Perforation shot locations estimated with contractor's velocity model and our simultaneous inverted velocity model. Ellipses are the 95 % confidence regions. Those estimated with our model are nearer to the real perforation shot locations comparing with those using the provided model. The right figure is the velocity model estimated with our simultaneous inversion (blue) and the one provided by the contractor (orange). The solid line is for V_p and the dashed line is for V_s .

Finally, we verified the microseismic event location with angle of incidence. Specifically, we first calculate the angle of incidence from P-wave polarization for each event station pair. Then, with the velocity model provided and that estimated by the simultaneous inversion algorithm, we respectively build a RMS angle of incidence misfit map for the event 2 of Figure 5. The misfit maps are shown in Figure 16 and Figure 17. From Figure 16, we can see that our inverted microseismic event location lies within an area of small angle of incidence residual. The RMS angle of incidence residual for this event is 8° . This means the microseismic event location and velocity model gives a prediction of P-wave polarizations that match the real data relatively well. However, the event location provided by the traditional method using the provided velocity gives a RMS angle of incidence residual of 18° (Figure 17). The real P-wave angle of incidence direction and the prediction at each station is shown in Figure 18. These comparisons show the locations estimated by the traditional method was unable to match the angle of incidence. Since the angle of incidence is independent of the arrival time information we used for inversion, it provides a good quality control (QC) check for microseismic event location which verified the accuracy of the event locations estimated by the simultaneous inversion algorithm.

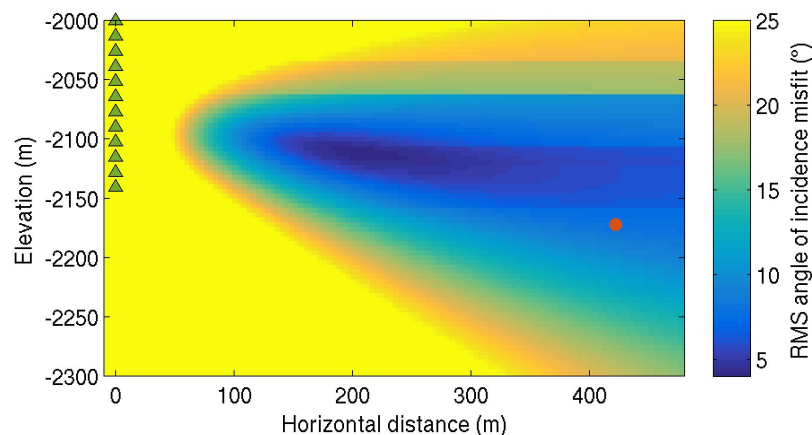


Figure 16: RMS angle of incidence misfit map for event 2 in Figure 5. The velocity model used is the one estimated with simultaneous inversion. The orange dot denotes the microseismic event location estimated by simultaneous inversion. It lies within an area of small angle of incidence residual.

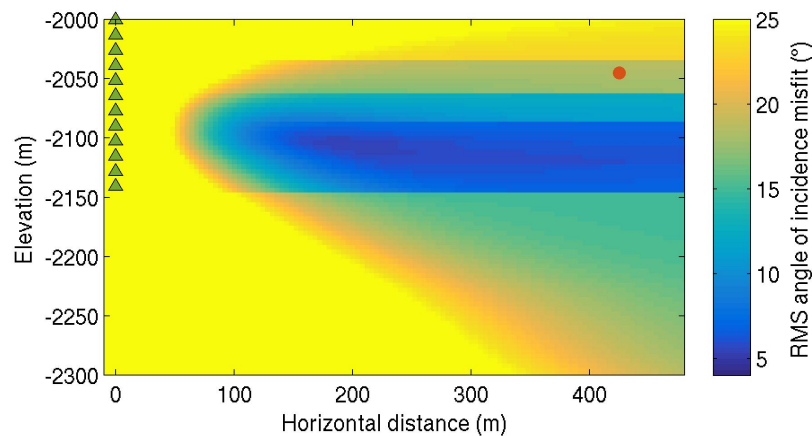


Figure 17: RMS angle of incidence misfit map for event 2 in Figure 5. The velocity model used is the one provided by the contractor. The orange dot denotes the microseismic event location estimated by the traditional method using the provided velocity model. It gives a relatively large angle of incidence residual of 18° .

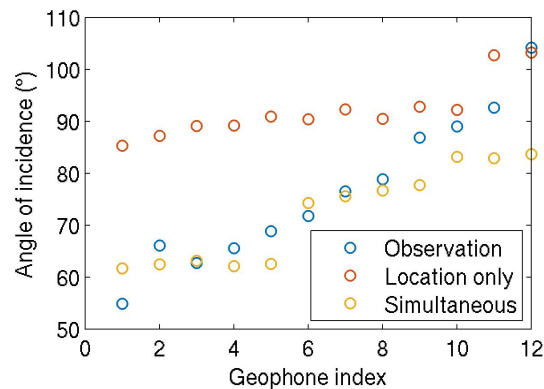


Figure 18: The real P-wave angle of incidence direction and the predictions at each station. The provided velocity model and the event location estimated with this velocity model result in relatively large difference from the real angles of incidence. The simultaneous inversion result is able to improve the match between the data and the prediction.

Stage 5

Similar with Stage 1, we locate the 55 microseismic events in Stage 5 with the velocity model provided by the contractor using traditional location method. The same with Stage 1, these two results are relatively similar. Figure 19 shows the location result of simultaneous inversion and the traditional location result using the provided velocity model. From the comparison, we can see the major difference between these two results lies in the event cluster 4 in Figure 19. The simultaneous inversion result is horizontally shifted towards the geophone array comparing with the other result using the provided velocity model.

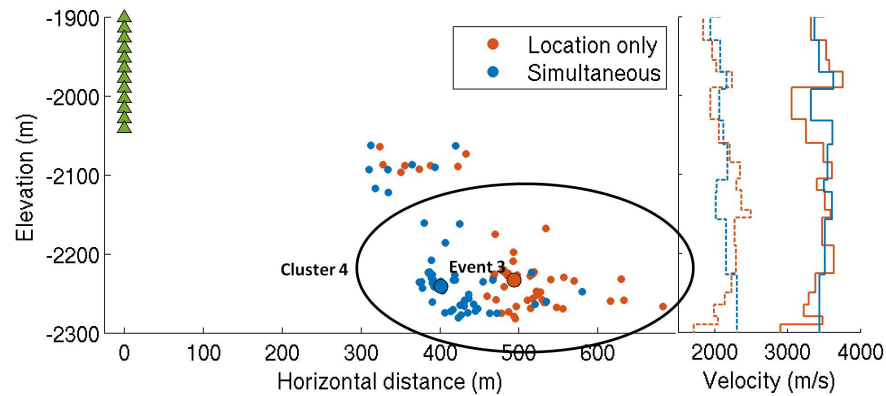


Figure 19: The same as Figure 5 but for the 55 events in Stage 5. There is a relatively large horizontal shift between these two results.

Figure 20 shows the arrival time comparison of event 3 in Figure 19. The traditional location method cannot fit the observed arrival time using the provided velocity model. The P- and S-wave moveouts of the “best” event location using the provided velocity model are apparently different from the real data, indicating that updating the velocity model is necessary. By constructing the velocity model with the simultaneous inversion, we were able to match the arrival times very well. Analyses with the same methods shown in Figure 13 and Figure 14 validate the effectiveness and stableness of the inversion. The result is not explicitly shown here for simplicity.

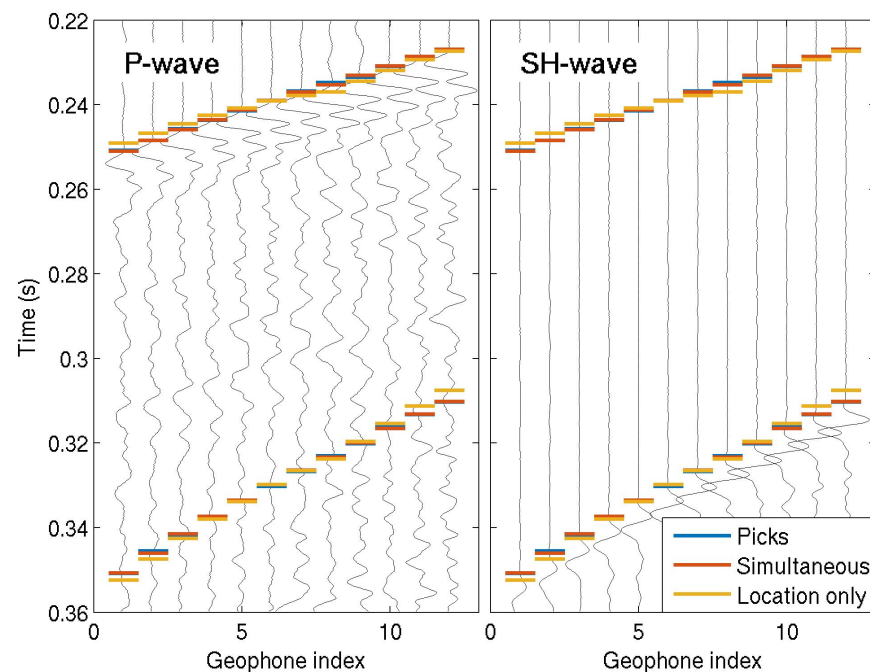


Figure 20: The same as Figure 6 and Figure 7 but for the event 3 in Figure 19.

Result of the entire data set

Finally, we show the simultaneous inversion result of all the detected microseismic events in Stage 1 and Stage 5. Here, we used the picks provided by the contractor instead of our own picks. We also added the azimuthal directions provided by the contractor using the horizontal components of P-wave polarization to show event location in 3D space. We located events from Stage 1A, Stage 1B, and Stage 5 separately. The result is shown in Figure 21 with the events color coded with their corresponding stages.

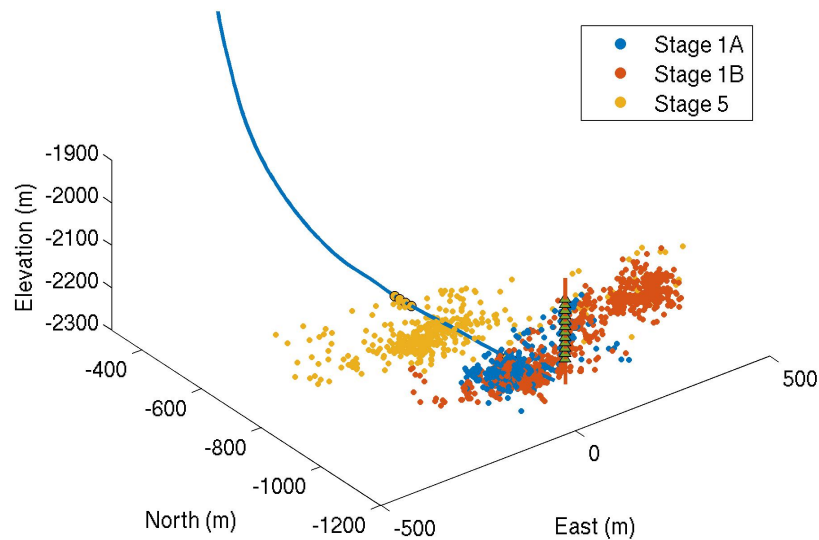


Figure 21: Microseismic event locations estimated by simultaneous inversion algorithm for Stages 1A, 1B, and 5. The events are color coded with their corresponding stimulation stages.

We also located the microseismic events with the velocity models provided by the contractor for each stage using the traditional location method. For the entire microseismic event set, the differences between the result of simultaneous inversion and the traditional method are similar with the differences obtained for the 76 and 55 events subsets from Stage 1 and Stage 5.

Figure 22 is the side view of the comparison for Stage 1B events. From this comparison, there is a vertical shift for a subset of events, which is consistent with the shift of Cluster 2 in Figure 5. Figure 23 and Figure 24 are respectively the event locations estimated with the traditional location method and simultaneous inversion color coded with their origin times. Comparing these two results, the events in Figure 24 estimated with the simultaneous inversion are more clustered, which might be an indication (but not necessarily) of more accurate event locations. Similarly, Figure 25 is the map view of the comparison for Stage 5 events. There is a horizontal shift of around 100 m, which is consistent with the shift of Cluster 4 in Figure 19. From Figure 26 and Figure 27, in which Stage 5 events are color coded with their origin times, we also found the events are more clustered for the simultaneous inversion result. Also, the two results lead to different interpretations. Figure 26 shows the early events occurred at the north side of the target stimulation zone, and gradually propagated to the south as the stimulation continues. Figure 27 shows the early events occurred at the south end of the target stimulation zone, and gradually propagate to south.

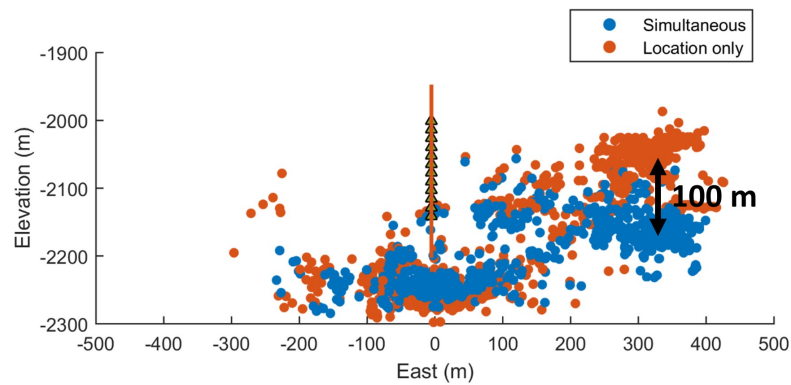


Figure 22: Side view of Stage 1B event locations estimated with the simultaneous inversion algorithm (blue dots) and those estimated with the provided velocity model using traditional method (orange dots). There is a vertical shift of around 100 m as shown in the figure. This is consistent with the shift of Cluster 2 in Figure 5.

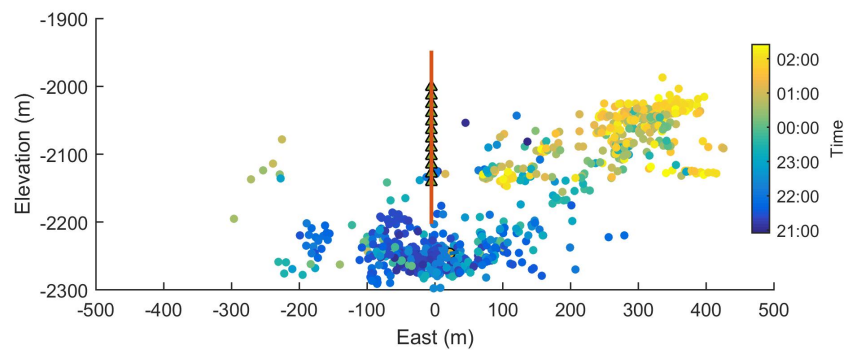


Figure 23: Side view of Stage 1B event locations estimated with the provided velocity model using traditional method. The events are color coded with their origin times. Comparing with the event locations in Figure 24, these events are more scattered.

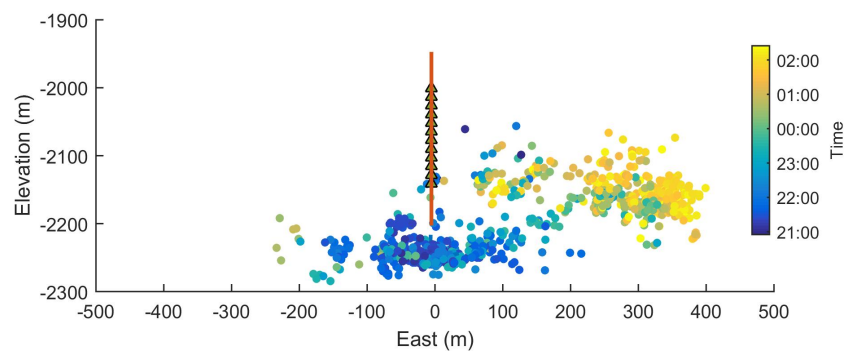


Figure 24: Side view of Stage 1B event locations estimated with the simultaneous inversion algorithm. The events are color coded with their origin times. Comparing with the event locations in Figure 23, these events are more clustered, which might be an indication (but not necessarily) of more accurate event locations.

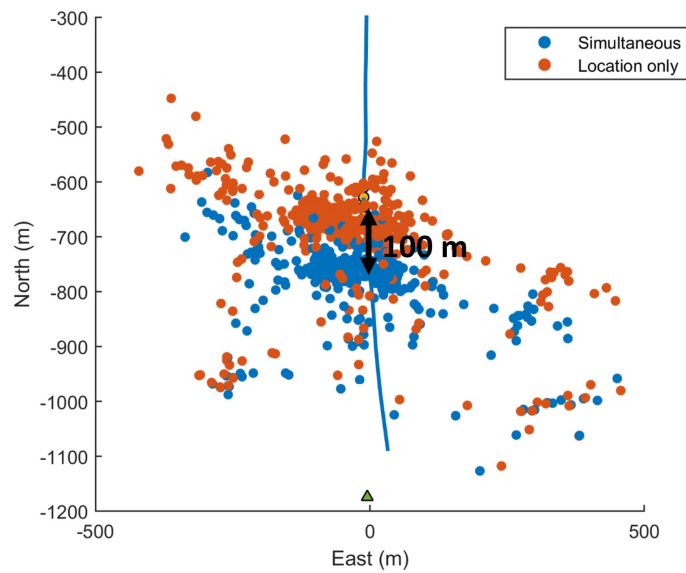


Figure 25: Map view of Stage 5 event locations estimated with the simultaneous inversion algorithm (blue dots) and those located with the provided velocity model using traditional method (orange dots). There is a horizontal shift of around 100 m as shown in the figure. This is consistent with the shift of Cluster 4 in Figure 19.

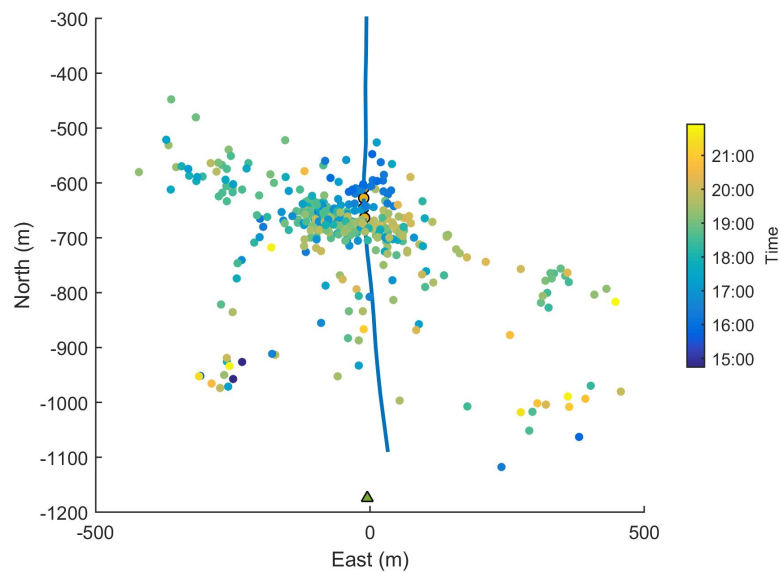


Figure 26: Map view of Stage 5 event locations estimated with the provided velocity model using traditional method. The events are color coded with their origin times. Comparing with the event locations in Figure 27, these events are more scattered.

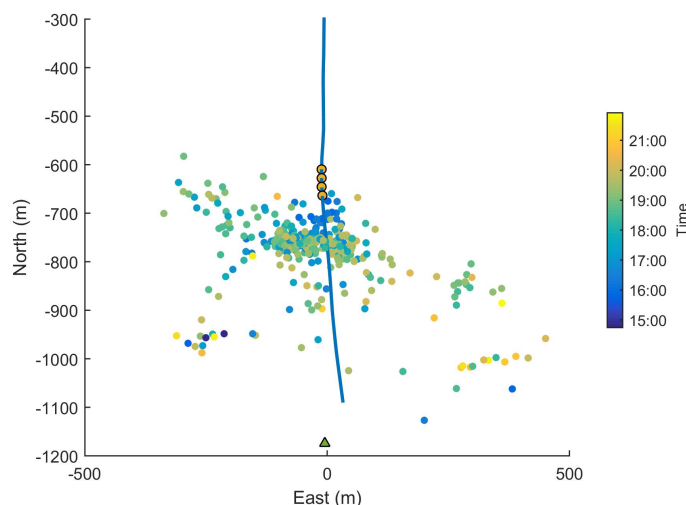


Figure 27: Map view of Stage 5 event locations estimated with the simultaneous inversion algorithm. The events are color coded with their origin times. Comparing with the event locations in Figure 26, these events are more clustered, which might be an indication (but not necessarily) of more accurate event locations.

Velocity model

One advantage of simultaneous inversion is the possibility to estimate variant velocity models for different subsets of data. We compared the velocity models estimated by the simultaneous inversion with different subsets of microseismic data and their associated V_p/V_s ratios in Figure 28.

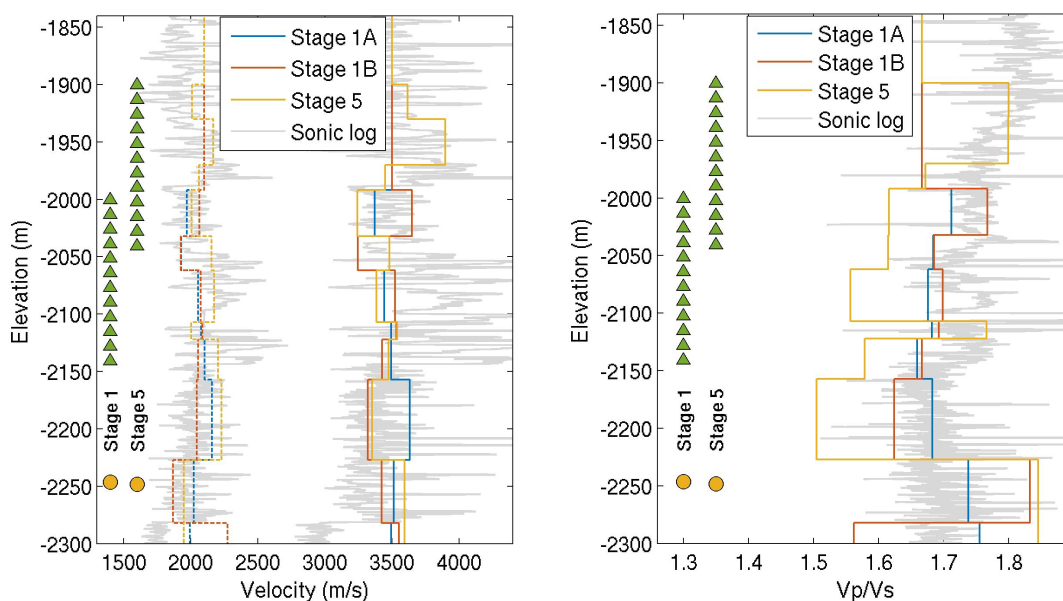


Figure 28: Left: velocity models estimated by the simultaneous inversion of the entire microseismic data set for each stage. Solid lines are for V_p and dashed lines are for V_s . Green triangles and yellow circle represent elevations of geophones and perforation shot for each stage. Right: V_p/V_s for each stage. Comparing the interval between the elevation of -2000 m and -2230 m, where there is a relatively good ray path coverage for both stages, the V_p/V_s is higher for Stage 5 than that of Stage 1.

The interval where there is relatively good ray path coverage for both Stage 1 and Stage 5 is between the elevation of -2000 m and -2230 m. From the comparison of the velocity models within this interval, the V_p/V_s is systematically lower for Stage 5 than that of Stage 1. One possible explanation to this change in the reservoir properties is introduced by hydraulic fracturing. Indeed, hydrofractures tend to result in low V_p/V_s or Poisson's ratio (Mavko et al., 2009). This is consistent with our simultaneously inverted velocity models. An alternative

explanation is the inherent lateral heterogeneity of the earth itself. Given the relatively large horizontal distance between Stage 1 and Stage 5, the property of the formation may change horizontally. Thus, further study need to be carried out to understand the cause of this change in the V_p/V_s (or Poisson's ratio).

Discussion

Velocity model is usually a major source of uncertainty for microseismic event location problem. However, various factors may dominate the location errors. The statics may cause a problem for highly weathered area in a surface microseismic survey. Anisotropy may need to be considered for specific sites. Thanks to the power of Bayesian inference, these factors may be accounted as model parameters depending on the necessity of a specific survey and availability of observations. The inclusion of these crucial parameters in the model to be estimated reduce the risk of bias introduced by inaccurate models. Also, various observations, such as P-wave polarization, shear wave splitting, reflected and refracted waves, can be used to help improve microseismic event location accuracy.

From this study, a stage dependent earth model is necessary due to either fracturing induced time-lapse change or horizontal heterogeneity of the formation. Simultaneous inversion provides the potential to construct data dependent velocity models given the abundance of microseismic events in most surveys. Integrated with rock physics models, the difference between various models can be used to characterize hydrofracture properties or horizontally heterogeneity of the formation. It may also be used to validate or calibrate a rock physics model.

Warpinski et al. (2009) have presented the evidence of anisotropy by showing the clear difference between the horizontal velocities measured from perforation timing and vertical log velocity for various shale formations. Preliminary research about anisotropic earth model parameters estimation have been carried out by Li, Zhang, Rodi and Toksoz (2013), Du and Warpinski (2013) with a VTI model and by Grechka, Singh and Das (2011) with homogeneous orthorhombic model. Although we do observe some clear shear wave splitting phenomena in the microseismic waveforms, the focus of this paper is to apply the simultaneous inversion method into the field case study using isotropic velocity model. Extending it to include anisotropy in the velocity model is our future work.

Conclusions

We simultaneously inverted for the velocity model and microseismic event locations in the Vaca Muerta Formation. The stability of the simultaneous inversion was tested with a cross-validation and the accuracy of the hypocenters was cross verified with P-wave polarization for looking at the event incidence angle at each receiver. The comparison with the traditional location result shows that simultaneous inversion provides a more effective way to use information from microseismic data to construct a velocity model. With this velocity model, microseismic event location accuracy can be significantly improved. With the algorithm demonstrated in this paper, we can not only perform microseismic monitoring to fracturing treatments where no perforation data is available; but also, improve the microseismic event location when we do have perforation data. In addition, this algorithm could be applied to long term reservoir monitoring where we can retrieve velocity information from the microseismic data themselves.

Acknowledgments

The authors thank Total S. A., Total Austral and its partners for granting permission to publish this paper.

References

- Aki, K., and P. G. Richards, 1980, *Quantitative Seismology: Theory and Methods*: WH Freeman and Company, San Francisco.
- Artman, B., I. Podladtchikov, and B. Witten, 2010, Source location using time-reverse imaging: *Geophysical Prospecting*, **58**, 861-873.
- Artman, B., and B. Witten, Year, Wave-equation microseismic imaging and event selection in the image domain: 2011 SEG Annual Meeting, Society of Exploration Geophysicists.
- Douglas, A., 1967, Joint epicentre determination: *Nature*, **215**, 47-48.
- Drew, J. E., H. D. Leslie, P. N. Armstrong, and G. Michard, Year, Automated microseismic event detection and location by continuous spatial mapping: SPE Annual Technical Conference and Exhibition, Society of Petroleum Engineers.

- Du, J., and N. Warpinski, 2013, Velocity building for microseismic hydraulic fracture mapping in isotropic and anisotropic media: Presented at the 2013 SPE Hydraulic Fracturing Technology Conference.
- Duncan, P., and L. Eisner, 2010, Reservoir characterization using surface microseismic monitoring: *Geophysics*, **75**, 75A139-175A146.
- Eisner, L., P. M. Duncan, W. M. Heigl, and W. R. Keller, 2009, Uncertainties in passive seismic monitoring: *The Leading Edge*, **28**, 648-655.
- Eisner, L., and J. H. Le Calvez, Year, New Analytical Techniques To Help Improve Our Understanding of Hydraulically Induced Microseismicity and Fracture Propagation: SPE Annual Technical Conference and Exhibition, Society of Petroleum Engineers.
- Gesret, A., N. Desassis, M. Noble, T. Romary, and C. Maisons, 2015, Propagation of the velocity model uncertainties to the seismic event location: *Geophysical Journal International*, **200**, 52-66.
- Grechka, V., P. Singh, and I. Das, 2011, Estimation of effective anisotropy simultaneously with locations of microseismic events: *Geophysics*, **76**, WC143-WC155.
- Jansky, J., V. Plicka, and L. Eisner, 2010, Feasibility of joint 1D velocity model and event location inversion by the neighbourhood algorithm: *Geophysical Prospecting*, **58**, 229-234.
- Li, J., C. Li, S. A. Morton, T. Dohmen, K. Katahara, and M. Nafi Toksöz, 2014, Microseismic joint location and anisotropic velocity inversion for hydraulic fracturing in a tight Bakken reservoir: *Geophysics*, **79**, C111-C122.
- Li, J., H. Zhang, W. L. Rodi, and M. N. Toksoz, 2013, Joint microseismic location and anisotropic tomography using differential arrival times and differential backazimuths: *Geophysical Journal International*, **195**, 1917-1931.
- Mavko, G., T. Mukerji, and J. Dvorkin, 2009, *The rock physics handbook: Tools for seismic analysis of porous media*: Cambridge university press.
- Maxwell, S., 2009, Microseismic location uncertainty: *CSEG Recorder*, **34**, 41-46.
- Maxwell, S., 2014, Microseismic imaging of hydraulic fracturing: Improved engineering of unconventional shale reservoirs.
- Myers, S. C., G. Johannesson, and W. Hanley, 2007, A Bayesian hierarchical method for multiple-event seismic location: *Geophysical Journal International*, **171**, 1049-1063.
- Myers, S. C., G. Johannesson, and W. Hanley, 2009, Incorporation of probabilistic seismic phase labels into a Bayesian multiple-event seismic locator: *Geophysical Journal International*, **177**, 193-204.
- Poliannikov, O. V., M. Prange, A. Malcolm, and H. Djikpesse, 2013, A unified Bayesian framework for relative microseismic location: *Geophysical Journal International*, ggt119.
- Poliannikov, O. V., M. Prange, A. E. Malcolm, and H. Djikpesse, 2014, Joint location of microseismic events in the presence of velocity uncertainty: *Geophysics*, **79**, KS51-KS60.
- Rutledge, J. T., and W. S. Phillips, 2003, Hydraulic stimulation of natural fractures as revealed by induced microearthquakes, Carthage Cotton Valley gas field, east Texas: *Geophysics*, **68**, 441-452.
- Song, F., and M. N. Toksöz, 2011, Full-waveform based complete moment tensor inversion and source parameter estimation from downhole microseismic data for hydrofracture monitoring: *Geophysics*, **76**, WC103-WC116.
- Tarantola, A., 2005, Inverse problem theory and methods for model parameter estimation: *siam*.
- Tarantola, A., and B. Valette, 1982, Inverse problems= quest for information: *J. geophys*, **50**, 150-170.
- Waldhauser, F., and W. L. Ellsworth, 2000, A double-difference earthquake location algorithm: Method and application to the northern Hayward fault, California: *Bulletin of the Seismological Society of America*, **90**, 1353-1368.
- Warpinski, N., 2009, Microseismic monitoring: Inside and out: *Journal of Petroleum Technology*, **61**, 80-85.
- Warpinski, N. R., C. K. Waltman, J. Du, and Q. Ma, 2009, Anisotropy effects in microseismic monitoring: SPE Annual Technical Conference and Exhibition, Society of Petroleum Engineers.
- Zhang, H., S. Sarkar, M. N. Toksöz, H. S. Kuleli, and F. Al-Kindy, 2009, Passive seismic tomography using induced seismicity at a petroleum field in Oman: *Geophysics*, **74**, WCB57-WCB69.
- Zhang, Z., B. Jafarpour, and L. Li, 2014, Inference of permeability heterogeneity from joint inversion of transient flow and temperature data: *Water Resources Research*, **50**, 4710-4725.
- Zhang, Z., J. W. Rector, and M. J. Nava, 2017, Simultaneous inversion of multiple microseismic data for event locations and velocity model with Bayesian inference: *Geophysics*, **82**, KS27-KS39.